PNAS RESEARCH ARTICLE | ENGINEERING NEUROSCIENCE

Artificial intelligence velocimetry reveals in vivo flow rates, pressure gradients, and shear stresses in murine perivascular flows

Kimberly A. S. Boster[a,1], Shengze Cai[b,1], Antonio Ladrón-de-Guevara[c], Jiatong Sun[a], Xiaoning Zheng[d], Ting Du[c,e], John H. Thomas[a], Maiken Nedergaard[c], George Em Karniadakis[f,g,2], and Douglas H. Kelley[a,2]

Edited by Arif Masud, UIUC; received October 18, 2022; accepted February 15, 2023 by Editorial Board Member Yonggang Huang

Quantifying the flow of cerebrospinal fluid (CSF) is crucial for understanding brain waste clearance and nutrient delivery, as well as edema in pathological conditions such as stroke. However, existing in vivo techniques are limited to sparse velocity measurements in pial perivascular spaces (PVSs) or low-resolution measurements from brain-wide imaging. Additionally, volume flow rate, pressure, and shear stress variation in PVSs are essentially impossible to measure in vivo. Here, we show that artificial intelligence velocimetry (AIV) can integrate sparse velocity measurements with physics-informed neural networks to quantify CSF flow in PVSs. With AIV, we infer three-dimensional (3D), high-resolution velocity, pressure, and shear stress. Validation comes from training with 70% of PTV measurements and demonstrating close agreement with the remaining 30%. A sensitivity analysis on the AIV inputs shows that the uncertainty in AIV inferred quantities due to uncertainties in the PVS boundary locations inherent to in vivo imaging is less than 30%, and the uncertainty from the neural net initialization is less than 1%. In PVSs of $N = 4$ wild-type mice we find mean flow speed 16.33 ± 11.09 μm/s, volume flow rate $2.22 \pm 1.983 \times 10^3$ μm^3/s, axial pressure gradient $(-2.75 \pm 2.01) \times 10^{-4}$ Pa/μm (-2.07 ± 1.51 mmHg/m), and wall shear stress $(3.00 \pm 1.45) \times 10^{-3}$ Pa (all mean ± SE). Pressure gradients, flow rates, and resistances agree with prior predictions. AIV infers in vivo PVS flows in remarkable detail, which will improve fluid dynamic models and potentially clarify how CSF flow changes with aging, Alzheimer's disease, and small vessel disease.

deep learning | perivascular space | particle tracking velocimetry | cerebrospinal fluid flow

Waste removal and nutrient delivery in the brain rely on flow of cerebrospinal and interstitial fluid (CSF and ISF) and play critical roles in brain health (1–7). Failures of this transport system, which have been linked to aging, stroke, and neurodegenerative diseases in mice (8–13) and humans (14–16), might be prevented and treated more effectively with better understanding of the fundamental mechanisms that govern CSF and solute transport (7). Failures of brain waste removal can allow formation of harmful plaques whose aggregation might be explained by quantifying transport rates and shear stresses. Analytic and computational models can enhance understanding but require accurate in vivo measurements of pressure and flow rate as inputs. For example, basic knowledge of pressure and flow rate has been used to validate simplified brain-wide models (17, 18). Similarly, local models hypothesizing the fluid dynamical mechanisms driving flow might also be validated or rejected if detailed, quantitative knowledge of pressure gradients were available.

In vivo measurements are possible and have provided valuable data, but have limits. CSF and ISF motion have been inferred brain-wide using optimal mass transport (19–21), but MRI, upon which the approach has been built, is limited by low spatial and temporal resolution. Fluid velocities in perivascular spaces (PVSs) surrounding arteries, which carry CSF into the deep brain regions, according to the glymphatic model (22, 23), have been measured with high resolution using particle tracking velocimetry (PTV) (12, 24–26), but the measurements are sparse and restricted to a single plane. Crucially, no existing in vivo methods have sufficient resolution to calculate accurate shear stresses, nor can they measure shear stresses directly, nor can they quantify pressure variations in PVSs.

To address these challenges, we introduce artificial intelligence velocimetry (AIV) to infer CSF flow fields in vivo. Recently, artificial intelligence has been applied extensively in fluid dynamics (27, 28), bringing insight to topics such as modeling and identification in computational fluid dynamics (29–32) and image processing in experiments (33, 34).

Significance

Diseases such as Alzheimer's and small vessel disease are linked to alterations of flow in the perivascular spaces that surround cerebral blood vessels and transport water-like fluids around brain tissue. Understanding the function, failure, and potential rehabilitation of the system depends on high-fidelity, in vivo quantification of flow rates, pressure, and shear stress, which have previously been unavailable. We show that artificial intelligence velocimetry (AIV), which integrates sparse two-dimensional (2D) in vivo velocity measurements with physics-informed neural networks, can accurately infer high-resolution pressure and shear stresses. AIV can also infer high-resolution three-dimensional (3D) velocities, thereby quantifying volume flow rates and resistances with high accuracy. Its unique capabilities make AIV a key tool for understanding brain fluid flow, toward improved clinical outcomes.

[1] K.A.S.B. and S.C. contributed equally to this work.

[2] To whom correspondence may be addressed. Email: d.h.kelley@rochester.edu or george_karniadakis@brown.edu.

This article contains supporting information online at http://www.pnas.org/lookup/suppl/doi:10.1073/pnas.2217744120/-/DCSupplemental.

Published March 29, 2023.

One artificial intelligence method, physics-informed neural networks (PINNs) (31, 35), can integrate sparse data with known equations of physics (36). Derived from PINNs, AIV (37) is designed to determine flow fields — including velocity, pressure, and shear stress — from sparse experimental measurements. AIV combines those measurements with known equations of motion to make inferences that match, as nearly as possible, both experiments and theory. Unlike simulations, AIV does not require that boundary conditions be fully known or that problems be well posed. It has been applied in vitro to infer velocity and stress fields of blood flow in a microchip (37). However, AIV has not yet been applied in vivo.

Here, we use AIV to infer three-dimensional (3D) flow fields in pial PVSs of mice with high temporal and spatial resolution. Our inferences are drawn from two-dimensional (2D) velocity measurements (u and v-velocity components only) from a single plane made with two-photon microscopy and particle tracking velocimetry (PTV). We train with 70% of the measurements and validate our results with the remaining unseen measurements, and we find good agreement. From the resulting 3D flow fields (u, v, and w velocity components in 3D space), we calculate pressure gradients, shear strain rates, shear stresses, volume flow rates, and hydraulic resistances, quantities which have never before been quantified with high fidelity from in vivo CSF flow measurements. Access to these quantities will improve efforts to model PVS flows and permit exploration of how these quantities change under various conditions, including aging and disease.

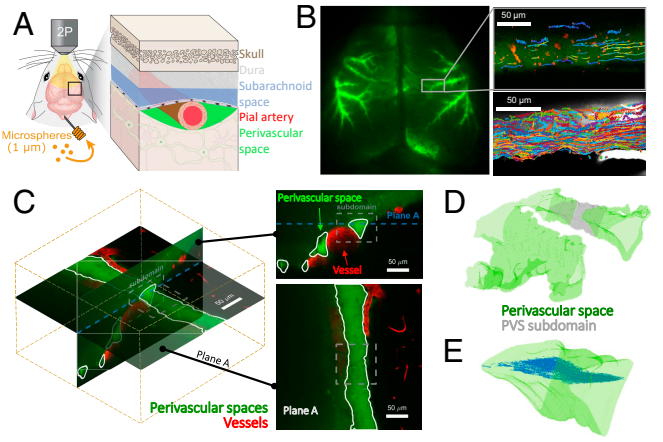

Fig. 1. Overview of two-photon imaging experiments and resulting data. (*A*) Two-photon microscopy with injected fluorescent one-micron microspheres and tracers enables visualization and quantification of the flow and perivascular space shape in a mouse brain. (*B*) Microsphere motion is determined using particle tracking velocimetry. Particle tracks in one plane at a single instant (*Top-Right*) and all tracks from a 1-min acquisition (*Bottom-Right*) are superimposed on a two-photon image. (*C*) A 3D image is reconstructed from a volume scan, with the perivascular space (PVS) boundaries outlined in white. The PVS and the vessel are visualized with different tracers, with the vessel shown here in red and the PVS in green. The blue dashed line indicates the location of the 2D imaging plane, labeled Plane A. The gray box indicates the location of the subdomain in which artificial intelligence velocimetry (AIV) is performed. (*D*) The PVS boundary is obtained by segmenting the image (*C*) based on fluorescence intensity. (*E*) A PVS subdomain is extracted for AIV analysis. Particle tracking locations are superimposed in blue.

Results

Quantifying 2D Velocity with Two-Photon Imaging of Fluorescent Microspheres. In order to visualize the PVS and quantify the flow of cerebrospinal fluid in a mouse brain, we injected fluorescent tracers (66.5 kDa Alexa Fluor 647–conjugated bovine serum albumin) and 1-micron microspheres into the cisterna magna of live, adult, wild-type mice anesthetized with ketamine/xylazine (100/10 mg/kg, intraperitoneally) (Fig. 1*A*), imaging with two-photon microscopy. Using PTV (24), we measured particle velocities, which track local fluid motion (Fig. 1*B*). Though two-photon microscopes can produce 3D images, recording at the speeds necessary for PTV is possible only in 2D, so we imaged on a plane of approximately uniform cortical depth, which we refer to as Plane A (Fig. 1*C*). With fluorescent tracers of different colors in blood and cerebrospinal fluid, we used 3D two-photon images to reconstruct the PVS boundaries based on the tracer intensity, as shown in Fig. 1 *C* and *D*. For subsequent AIV analysis, we focus on a typical subdomain, as shown in Fig. 1*E* with particle locations indicated. In this paper, we present results from $N = 4$ wild-type mice. More details can be found in *Methods*. In pial PVSs, fluid pulses in tight synchrony with the cardiac cycle (24), so we reduced the effective sparsity of particles by merging PTV measurements from many cardiac cycles, according to the instantaneous phase of each cycle, as illustrated in *SI Appendix*, Fig. S1 and further described in *Methods*.

3D Flow Fields. In AIV, a fully connected neural network takes the time and space coordinates (t, x, y, z) as inputs and infers the three velocity components (u, v, w) and pressure (p) as illustrated in Fig. 2*A*. The parameters in the neural network (Θ) are trained by minimizing the mismatch between the network predictions and PTV data $(\mathcal{L}_{data})$, while simultaneously minimizing the residuals of the Navier–Stokes equations $(\mathcal{L}_{res})$ and the no-slip boundary conditions on the PVS surfaces $(\mathcal{L}_{bcs})$. More details about the AIV algorithm can be found in *Methods*. For an initial validation, we performed a direct numerical simulation of CSF flow in a similar PVS domain, using a subset of simulation results (u and v-velocity components from a single plane) to train an AIV model, then compared its inferences to the remaining simulation results. The relative errors of the inferred velocity and pressure fields were approximately 5% (*SI Appendix*, Figs. S2 and S3).

For further validation, we trained the AIV model using 70% of the PTV measurements from each mouse and validated the AIV-inferred velocities on the remaining PTV measurements. The results for mouse 1 are shown in Fig. 2 *B* and *C*: Velocity vectors and distributions inferred by AIV are consistent with those of PTV, indicating that the AIV is well trained and accurate. The Rms error and the root-median-square error between PTV and AIV for mouse 1 are 13.08 μm/s and 7.16 μm/s, respectively, which correspond to percent errors of 25.63% and 25.24%, respectively. For reference, we estimate the velocity measurement error in PTV to be 1.9 μm/s (*SI Appendix*). Fig. 2*D* shows a comparison between phase-merged PTV measurements, which are made only at the disordered locations of particles, and AIV inferences, which we show on a regular grid. From four snapshots shown in the figure, it is clear that AIV accurately captures the two flow reversals occurring during a cardiac cycle. The spatial root-mean-square (RMS) velocity and spatially averaged downstream velocity for PTV and AIV generally agree (Fig. 2*E*). Comparing the time-averaged, normalized velocity for AIV and PTV in Plane A, shown in *SI Appendix*, Fig. S11*D* demonstrates that AIV accurately captures spatial variation. Because in vivo PTV measurements, even after phase merging, are more sparse than AIV inferences, we calculate mean speeds in larger regions when considering PTV and when comparing it to AIV. The velocity field in Plane A, where the PTV observations used for training were made (*SI Appendix*, Fig. S11*D*), is smooth along the length of the PVS subdomain and similar to that in Plane B, a different plane from the location of the PTV observations

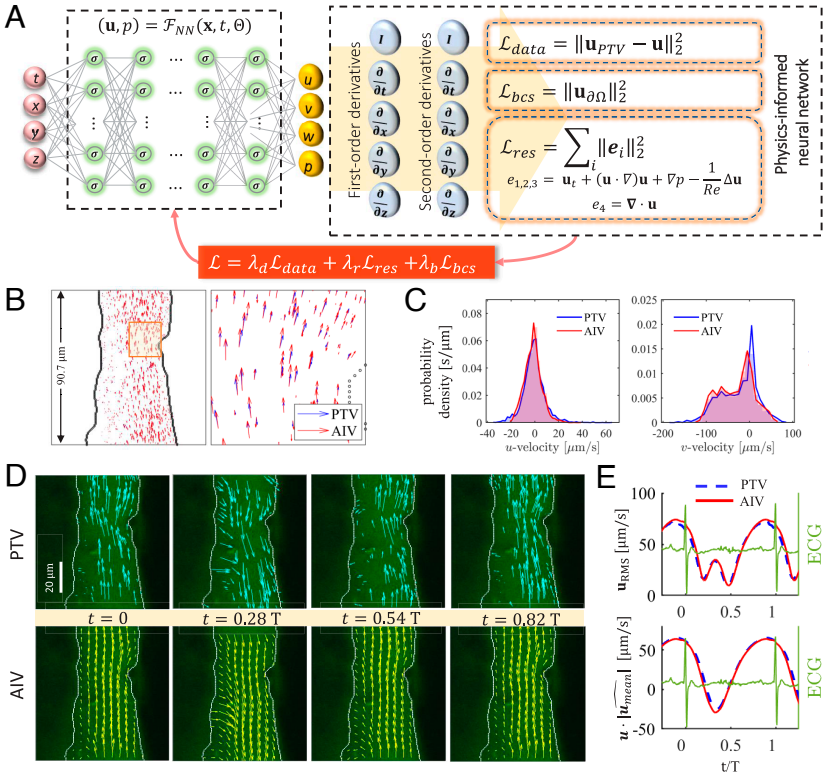

Fig. 2. AIV infers 3D high-resolution velocity from boundaries and 2D particle tracks. (*A*) A schematic diagram of artificial intelligence velocimetry (AIV), which can infer 3D flow fields from 2D particle tracks. (*B* and *C*) Comparison between particle tracking velocimetry (PTV) measurements and AIV-inferred velocities of the validation data, where (*B*) shows phase-merged vector fields and (*C*) shows histograms of two velocity components, including data from the entire duration analyzed. (*D*) Comparison between time-series phase-merged PTV data and AIV-inferred velocity fields in Plane A. Four snapshots are shown; *T* is the cardiac cycle duration, typically about 30 ms. (*E*) Rms velocity (*Top*) and downstream velocity (*Bottom*) from PTV (blue) and AIV (red). ECG signals indicate cardiac activity.

used for training (*SI Appendix*, Fig. S11*C*), suggesting that AIV is not overfitting the data. By combining the Navier–Stokes equations, 3D boundary conditions, and 2D PTV measurements, AIV infers the 3D velocity fields. *SI Appendix*, Fig. S11*B* shows the time-averaged 3D speed (calculated from all three velocity components) in three planes.

Volume Flow Rate. PTV from two-photon images provides velocities in a single plane, but volume flow rate is the more directly relevant quantity for mass transport. If the imaging plane used for PTV is not close to the center of the PVS, or the measurement locations are more dense in the center of the PVS where the flow is faster, the measured velocities will not reflect the average velocity in the entire PVS, whereas measuring the volume flow rate directly avoids those challenges. Volume flow rates have been estimated based on average velocity measurements from a single plane and estimates of the 3D geometry previously (17), but never directly measured. AIV infers the time-varying volume flow rate in perivascular spaces with fewer assumptions regarding the geometry. Fig. 3*A* shows the volume flow rate through cross-sections we label as the inlet and outlet, over the course of a cardiac cycle. The ratio of oscillatory-to-net flow for mouse 1 is 3.7. Among $N = 4$ mice, the time-averaged volume flow rate at the inlet ranged from 0.5 to 5 $\times 10^4$ $\mu m^3/s$, and the difference between the time-averaged flow rates at inlet and outlet ranged from −12 to 33%, as reported in Table 1. A negative value indicates that more fluid passes the outlet than the inlet. In principle, conservation of mass would lead us to expect the inlet and outlet flow rates to match exactly. In practice, a small mismatch is expected, because AIV enforces mass conservation locally but not globally. We find a ∼2% mismatch when applying AIV to simulation results, as shown in *SI Appendix*, Fig. S2. There are no penetrating vessels branching from the pial vessels in any of the subdomains in which AIV is performed. Mouse 2 and mouse 4 had the largest difference between the inlet and outlet flow rates, and in those mice we see evidence of flow outside of the region defined as the PVS at the exact location along the length of the PVS where the volume flow rate changes (*SI Appendix*, Fig. S5). We describe possible implications of this finding more in *Discussion*.

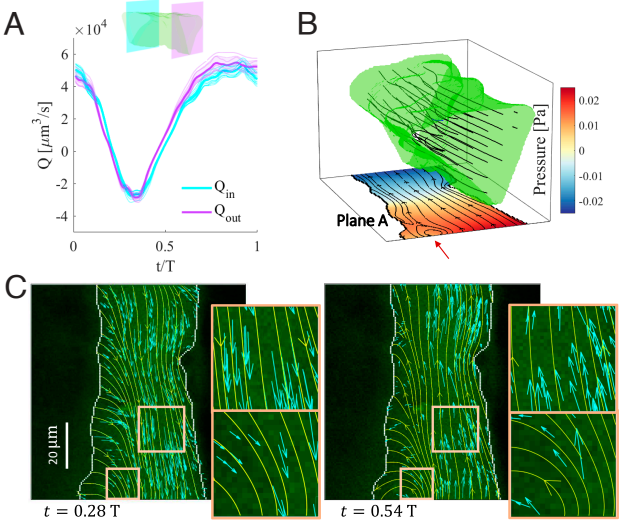

Fig. 3. AIV reveals volume flow rate and flow structures. (*A*) Volume flow rates through the inlet and outlet over the course of one cardiac cycle. Inferences from six different boundary shapes (all in mouse 1) are shown as faint curves; their mean and deviation are indicated with bold curves and shaded regions, respectively. (*B*) Inferred streamlines of the time-averaged velocity field. A 2D projection on Plane A is shown with the streamlines superimposed on the pressure field. A potential small vortex is observed from the streamlines, as indicated with an arrow. (*C*) Inferred streamlines (yellow) agree well with PTV measurements (cyan). Two snapshots immediately after changes in flow direction are shown, and enlargements show the regions marked with pink boxes.

AIV-Inferred Streamlines Capture Flow Structures. Streamlines are useful for visualizing flow structures that may arise from irregularly shaped boundaries, such as large amyloid deposits. Streamlines can be calculated with great accuracy from the high-resolution flow fields inferred by AIV. Fig. 3*B* shows streamlines of the mean velocity in mouse 1. The flow is mostly unidirectional, but a small vortex can be observed near one boundary. Plotting streamlines together with PTV measurements (Fig. 3*C*) shows good agreement: The particles in the *Bottom-Left* region move differently from those in the main flow region. However, because flow in PVSs is laminar (24), we would not expect turbulent vortices. One possible reason for vortex formation is the interaction of the downstream flow with the oscillatory cross-stream flow induced by pulsing artery walls. As shown in Fig. 3*C*, the streamlines close to the left wall (the pulsing vessel) are nearly normal to the wall, not parallel to it, like the streamlines of the mean flow (Fig. 3*B*). The two snapshots in Fig. 3*C* were taken when the flow changes direction, so the cross-stream motion may result from that reversal. However, because the flow is laminar, we would expect short-lived flow structures resulting from the downstream pulsatility to average out in the time-averaged flow. Another possible explanation for the vortex might be the upstream presence of aggregated microspheres or the presence of native structures or cells, such as epipial cells (38) or perivascular macrophages (39). Careful examination of the original images did not reveal aggregated microspheres or biological structures, but they may be located above or below the imaging plane, and the biological structures may be invisible because they do not interact with tracers or microspheres. If the PTV measurements are not weighted heavily enough in the loss function, or the particles on the left side of the image are excluded during training, the vortex disappears from AIV inferences (*SI Appendix*, Fig. S7), confirming that AIV is correctly incorporating PTV measurements. Whatever the cause of vortices, they are likely to promote transport in the PVS.

Pressure. In vivo imaging reveals anatomical structures and fluid motion. Methods such as PTV and optimal mass transport quantify that motion as it varies over space and time (19–21). The forces and stresses driving that motion, however, have been essentially impossible to measure in PVSs. AIV allows us to obtain in vivo pressure fields in PVSs. The time-averaged pressure in mouse 1, shown in Fig. 4*A*, decreases smoothly from inlet to outlet, as expected for a flow subjected only to viscous and pressure forces. Similarly, instantaneous pressure fields decrease smoothly along the direction of flow (Fig. 4*B*).

Fig. 4*C* shows the spatially averaged pressure as it varies over the course of the cardiac cycle. The ratio of oscillatory-to-net pressure is 3.3 for mouse 1. Fig. 4*D* shows the temporally averaged pressure and axial pressure gradient as they vary along the length of the PVS. The pressure varies approximately linearly. The pressure gradient $\partial P/\partial n$ is larger where the PVS narrows, as would be expected since hydraulic resistance R scales with the inverse square of the cross-sectional area ($R \propto A^{-2}$) for purely axial flow, and off-axial flow components induced by the changing cross-sectional shape and area increase R further. The average pressure gradients in the axial direction n ranges from 0.7 to 5×10^{-4} Pa/μm for the $N = 4$ different mice, as shown in Table 1.

Shear Stress. Wall shear stress is important in cardiovascular flows (40–46), and has been hypothesized to be important in lymph vessels (47, 48). Wall shear stress is a mechanical

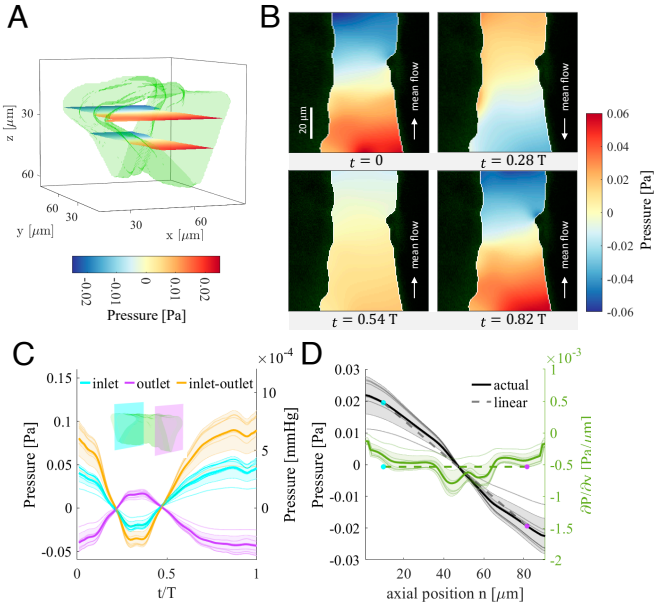

Fig. 4. AIV infers 3D high-resolution pressure. (*A*) Time-averaged pressure (shown on two planes) in the PVS subdomain inferred by AIV. (*B*) Four snapshots of the pressure in Plane A during a cardiac cycle. *T* is the cardiac cycle duration. (*C*) Spatially averaged pressure at planes near the inlet and outlet of the subdomain, as depicted in the inset, during one cardiac cycle, along with the pressure difference. Inferences from six different boundary shapes (all in mouse 1) are shown as faint curves; their mean and deviation are indicated with bold curves and shaded regions, respectively. (*D*) Temporally averaged pressure (black) and pressure gradient (green) along the length of the PVS subdomain. Dots locate the inlet and outlet. Dashed lines show a hypothetical uniform pressure gradient, for reference.

signal sensed by the tissue at PVS boundaries that may cause cellular responses affecting flow and transport, as it does in blood flow (40–46). It is unclear what role shear may play in PVS flows, but AIV allows us to obtain in vivo shear stress fields in PVSs. To validate that AIV can infer shear stress with reasonable accuracy, we compared the shear stress calculated in the direct numerical simulation of CSF flow in a PVS domain with that inferred by AIV using a subset of the simulation results (*SI Appendix*, Figs. S2 and S3). The AIV-inferred shear stress agrees reasonably well with shear stress in the simulation (L2-norm of error of 13.92%). The time-averaged and fluctuating shear stress at the wall inferred in mouse 1 are illustrated in Fig. 5 *A* and *B*, respectively. We report shear stress magnitude at the wall, calculated from the second invariant of the stress tensor (*Methods*), not the single component of the tensor, which indicates streamwise stress on the boundary surface and is often called "wall shear stress". The magnitude, not the single component, is likely to be the relevant quantity for aggregation and mechanical signaling.

Fig. 5*C* shows the spatially averaged and spatially maximum shear stress at the wall over the course of a cardiac cycle. The ratio of oscillating to average shear stress is 1.3 for mouse 1. Among all four mice, the mean shear stress varied from 1.48 to 4.95×10^{-3} Pa, as listed in Table 1. Fig. 5*D* shows how the temporally averaged shear stress at the wall varies along the length of the PVS. The axial variation approximately corresponds to changes in the PVS cross-sectional area, with larger shear stresses where the channel is narrower, as we would expect. In fact, if we consider a reference location with cross-sectional area A_0 and shear stress at the wall τ_0, the shear stress at the wall at any other location, with cross-sectional area A, can be accurately approximated as $\tau_0(\frac{A_0}{A})^{\frac{3}{2}}$, as shown in Fig. 5*D*. Our reasoning for this approximation is given in *SI Appendix*.

Table 1. Quantities of interest for each mouse

Mouse	PTV $u \cdot \hat{u}_{\text{mean}}$ (μm/s)	$\frac{Q}{A}$ (μm/s)	Q (μm^3/s)	$\frac{Q_{in}-Q_{out}}{Q_{out}}$	$\dot{\gamma}$ (1/s)	$\frac{\partial P}{\partial n}$ (Pa/μm)	$\frac{\partial P}{\partial n}$ mmHg/m	R (Pa·s/μm^4)	Shear stress at walls (Pa)
1	19.76	20.15	2.18×10^4	−0.12	4.53	-5.34×10^{-4}	−4.02	2.49×10^{-8}	4.95×10^{-3}
2	14.76	29.98	5.02×10^4	0.33	2.12	-3.25×10^{-4}	−2.44	6.47×10^{-9}	3.16×10^{-3}
3	7.78	10.38	1.13×10^4	0.00	1.69	-1.70×10^{-4}	−1.23	1.51×10^{-8}	2.30×10^{-3}
4	6.38	4.80	5.57×10^3	0.33	1.00	-7.26×10^{-5}	−0.546	1.30×10^{-8}	1.58×10^{-3}
mean	12.17	16.33	2.22×10^3	0.14	2.33	-2.75×10^{-4}	−2.07	1.49×10^{-8}	3.00×10^{-3}
σ	6.25	11.09	1.983×10^3	0.23	1.53	2.01×10^{-4}	1.51	7.63×10^{-9}	1.45×10^{-3}

All values except the shear rate are temporally and spatially averaged. The shear rate is the median of all points in time and space. The values reported for mouse 1 are the average of the predictions from G1 to G6.

Whereas shear stress is the force (per unit area) inducing adjacent material elements to slide past each other, the rate at which they slide past each other is the shear strain rate, and we calculate it from spatial velocity derivatives inferred via AIV. Large shear strain rates in bulk CSF flows have been hypothesized to promote formation of harmful plaques in the brain (49–51). Fig. 5*E* shows the inferred shear strain rate as it varies over space and time.

Inertial Forces Are Negligible in Perivascular Flows. The Reynolds number Re is a dimensionless measure of the ratio between inertial and viscous forces in a flow and is defined as $Re \equiv \frac{UL}{\nu}$ where U is a typical flow velocity, L is a length scale for spatial variations in the flow velocity, and ν is the kinematic viscosity. For a pulsatile flow, an important parameter is the dynamic Reynolds number Rd (related to the Womersley number Wo), a dimensionless expression relating the pulsatile flow frequency ω to viscous effects, defined as $Rd \equiv Wo^2 \equiv \frac{\omega L^2}{\nu}$. If we take U = 20 μm/s average downstream CSF speed in pial PVSs (24), ω = 5 Hz (approximate murine cardiac frequency), L = 40 μm (approximate PVS width), and $\nu = 7\times10^{-7}$ m^2/s (water at 37 °C), then $Re = 1.1\times10^{-3}$ and $Rd = 1.1\times10^{-2}$. In the Navier–Stokes momentum equation (Eq. **2**), we expect the nonlinear inertial term to scale with Re and the unsteady acceleration term to scale with Rd, as we show in *SI Appendix*. Thus, we predict that the unsteady term ($\partial\mathbf{u}/\partial t$) has small magnitude compared to the viscous and pressure terms ($\nu\nabla^2\mathbf{u}$ and $-\nabla p/\rho$, respectively), and that the nonlinear term ($\mathbf{u}\cdot\nabla\mathbf{u}$) is even smaller. With the high-resolution velocity and pressure fields inferred by AIV, we can calculate each term in vivo. The unsteady term, the inertial term, and the sum of the viscous and pressure terms, all spatially averaged and varying over one cardiac cycle, appear in Fig. 6*A*. As predicted, the nonlinear inertial term is negligible, and the viscous and pressure terms have individual amplitudes (not shown) much larger than the unsteady term. Time variations in the flow velocity are in phase with time variations in the pressure field. We also note that the residual of the Navier–Stokes equation is not exactly zero, as there exists minimization and approximation error in AIV which cannot be totally avoided. The resulting flow field is a trade-off between the experimental data and the governing equations. In summary, we find that for the flow determined by AIV, the nonlinear inertial term $(u\cdot\nabla)u$ is indeed negligibly small, a fact that simplifies modeling considerably and makes reduced order network models (like those in refs. 18, 52 and 17) reasonable.

Hydraulic Resistance. The hydraulic resistance (per unit length) $R \equiv \frac{\partial P/\partial n}{Q}$, where Q is the volume flow rate, is a convenient parameter in modeling PVS fluid flow. Using AIV, inferences of pressure gradient and flow rate to calculate the hydraulic resistance directly, we found $0.6 \le R \le 2.5\times10^{-8}$ Pa·s/μm^4 for the different mice, as reported in Table 1. To validate, we performed a direct numerical simulation of steady flow through shape G1, shown in *SI Appendix*, Fig. S4. The hydraulic resistance calculated using simulation data agrees within 0.5% with that inferred by AIV.

Pressure gradients and flow rates have been unavailable previously, so resistance has been estimated using assumptions about the PVS shape and flow (17, 18, 52, 53). Specifically, previous models estimated resistances by assuming Poiseuille flow in idealized shapes with uniform cross-sections, which results in unidirectional axial flow governed by Poisson's equation. To put the resistance inferred from AIV in context, we estimated R for shape G1 using a similar approach but accounting for spatial variation of PVS cross-section: We determined the cross-sectional shape at many locations along the PVS, solving Poisson's equation to determine R for each. The results are labeled "exact" in Fig. 6*B*. Because the shape and area vary along the PVS, we obtain a distribution of resistances; the mean and deviation are shown. We also calculated the resistance for circular and elliptical half-annular segments with cross-sectional areas matching the exact segments. We used the half-annular shape because the subdomain included only one side of the PVS, as shown in Fig. 1 *C* and *D*. Results were similar to the "exact" case. We also report the resistance per unit length for the other geometries from mouse 1 (G2–G6) in Fig. 6*B*. The hydraulic resistance is very sensitive to uncertainties in the PVS geometry because it scales inversely with the square of the area, or with the length scale to the fourth power. The resistance inferred by AIV is 9.2% larger than the median resistance and 10.9% larger than the mean resistance in channels with uniform cross-section and the exact shape. Solving Poisson's equation probably yields artificially small resistances because it neglects off-axial velocity components induced by the varying cross-section. However, the discrepancy is only ∼10%, much less than changes to R caused by variations in boundary shape associated with threshold choices (shapes G2–G6 in Fig. 6*B*) or the changes in R caused by variations in shape and area along the length of the PVS. The uncertainty associated with the PVS boundary is larger than the error that results from neglecting off-axial flow components. Thus, assuming a straight cross-section and idealizing it as an elliptical annulus are reasonable approximations.

Sensitivity Analysis. AIV inferences depend on the governing equations, the AI training parameters, and the experimental measurements, including PTV velocities and 3D boundary positions. Though AI parameters are refined iteratively in the

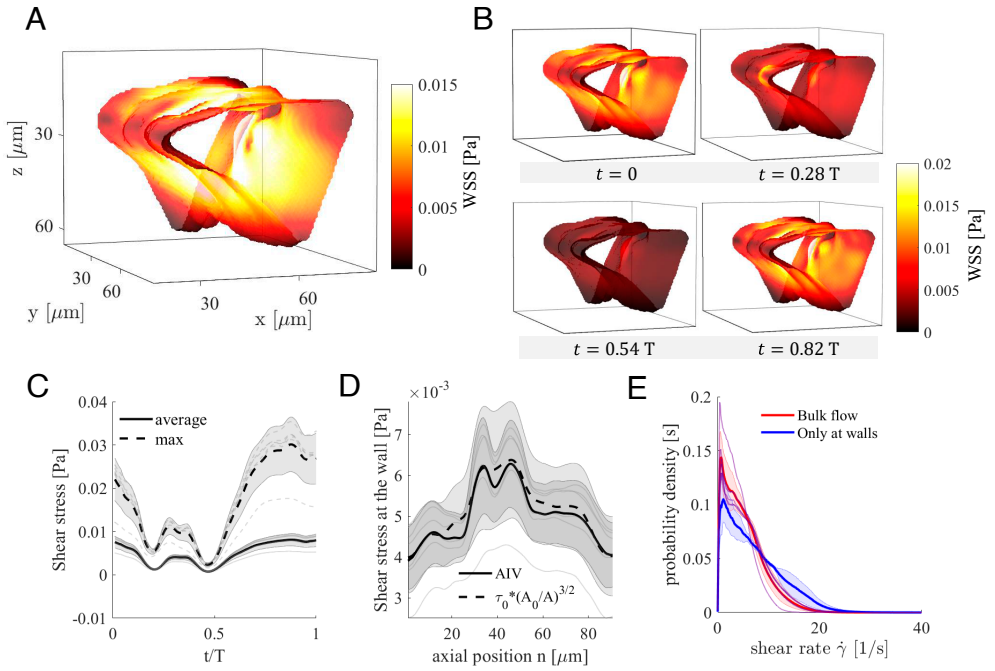

Fig. 5. AIV infers 3D high-resolution shear stress. (*A*) Time-averaged shear stress at the wall in the PVS subdomain, inferred by AIV. (*B*) Four snapshots of shear stress at the wall in the PVS subdomain during a cardiac cycle; *T* is the cardiac cycle duration. (*C*) Spatially averaged and spatially maximal shear stress at the wall in the PVS subdomain during one cardiac cycle. Inferences from six different boundary shapes (all in mouse 1) are shown as faint curves; their mean and deviation are indicated with bold curves and shaded regions, respectively. (*D*) Temporally and spatially averaged shear stress at the wall along the length of the PVS. The dashed curve shows the shear stress predicted by Eq. **2**. (*E*) Distributions of shear rates from every point in the flow (red) and at the walls (blue).

training process, their initial values must be chosen manually and might affect inferred quantities. Considering measured quantities, the uncertainty associated with any single PTV measurement is small because we typically record thousands and because each has submicron accuracy in the transverse plane. In contrast, location of the 3D PVS boundaries is based on a single measurement and is weighted higher (twice as heavily as the particle tracking measurements), in order to confine the flow in a specific 3D domain and provide the boundary conditions. This allows us to infer the 3D flow fields from 2D measurements but affects the inferred quantities such as volume flow rate. We performed a sensitivity analysis to determine the impact of the PVS boundaries and AIV initialization on the inferred quantities.

We trained the neural network five times, each with slightly different initial parameter values, and compared the independent AIV inferences for pressure, flow rate, and shear, finding variation less than 1% in most cases (*SI Appendix*, Fig. S6), showing that the inference is largely independent of the neural network initialization.

Though we can determine the PVS boundary location with good accuracy based on the tracer injected into the PVS, challenges inherent in segmentation introduce some uncertainty. We vary the parameters used to determine the PVS boundary to produce six different PVS shapes, referred to as G1–G6, that are intended to bracket the real location of the boundary. This process is described further in *Methods* and *SI Appendix*, Fig. S4.

The dependence of pressure, pressure gradient, volume flow rate, shear rate, and hydraulic resistance on uncertainty in the PVS boundaries is shown in Figs. 3*A*, 4 *C* and *D*, 5 *C*–*E*, and 6*B*. The inferred quantities are similar for all of the shapes except G3, where they differ by more than a SD. The uncertainty in pressure, volume flow rate, and shear stemming from the uncertainty in the PVS boundaries is generally less than 30%. These quantities of interest are considerably more sensitive to the 3D boundaries than to the AI initialization parameters, as shown in *SI Appendix*, Fig. S6, highlighting the robustness of the AIV training. An uncertainty less than 30% is reasonable and considerably better than existing approaches for measuring or estimating pressure, flow rates, and wall shear stress. Furthermore, the uncertainty in 3D boundary locations could be reduced with different imaging. In this work, boundary locations are determined from tracer fluorescence in the PVS. However, fluorescent intensity depends on tracer concentration, which varies over space and time. Boundary uncertainty might be reduced by visualizing the PVS walls, rather than the lumen as indicated by tracer, by imaging transgenic mice where the collagen in the PVS walls are labeled with green fluorescent protein.

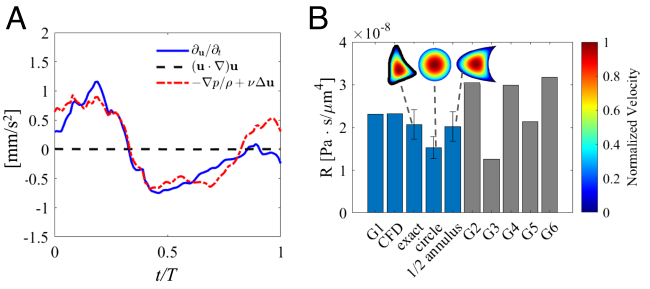

Fig. 6. AIV reveals inertial contribution and hydraulic resistance in glymphatic flow. (*A*) Spatial averages of terms in the Navier–Stokes equation, computed from the inferred flow field. The nonlinear term $(\mathbf{u}\cdot\nabla)\mathbf{u}$ is much smaller than the others and can be accurately neglected. (*B*) Hydraulic resistance determined by AIV for the six different shapes G1–G6 (*SI Appendix*, Fig. S4), and hydraulic resistance for geometry G1 determined in four different ways: direct simulation (CFD), Poiseuille flow through straight channels with exact cross-sectional shapes (exact), Poiseuille flow through circular channels with matching cross-sectional areas (circle), and Poiseuille flow through half-annuli with matching cross-sectional areas (1/2 annulus). The cross-sectional shapes vary along the PVS; error bars indicate ± 1 SD. The normalized (by the maximum velocity) velocity profile in one-sample cross-section is shown for each of the straight-channel scenarios.

Discussion

We demonstrate that AIV can infer 3D velocity fields of cerebrospinal fluid in perivascular spaces, in vivo, at resolution previously possible only in simulations, from 2D particle tracks. AIV also provides in vivo time-varying pressure, pressure gradients, volume flow rate, and wall shear stress —quantities

which have previously been practically inaccessible, except in simulations. Unlike simulations, AIV does not require that problems be well posed or that inlet and outlet boundary conditions be known (as is difficult or impossible in vivo). Sensitivity analysis shows that AIV inferences vary less than 1% with different neural net initial conditions and less than 30% with different PVS boundary segmentations. We confirm that the inertial term in the momentum equation can accurately be neglected, simplifying modeling efforts. The hydraulic resistances we infer by AIV and validate by computational fluid dynamics are larger than for unidirectional Poiseuille flow; off-axial flow arising from variations in PVS cross-section increases resistance by about 10%, less than does uncertainty of boundary shape, a fact useful for modeling.

AIV-inferred velocities agree with PTV and previous measurements. Comparing AIV inferences to PTV measurements, Rms and root-median-square velocity errors ranged from 5 to 13 and 3 to 7 μm/s, respectively, for the different mice —less than 1 pixel/frame (≈19 μm/s). The good agreement suggests that the pial PVSs we measure are open, not porous, as has been shown previously (25), since the Navier–Stokes equations we enforce apply to open domains. The average downstream velocities we measured with PTV and inferred with AIV are comparable to measurements reported previously (24, 54, 55).

In contrast to particle tracking, AIV provides the average velocity in the entire 3D PVS. Particle tracking velocimetry has provided invaluable insight into the presence and rates of flows in PVSs, but it provides only velocity information in a single plane. In Table 1, we report the average downstream velocity calculated based on the particle tracks (in a single plane) and the average velocity in the entire 3D PVS, inferred via AIV. For three of the four cases, the average velocity in the 3D PVS is within ∼25% of the average from PTV. However, the average velocity in the 3D PVS is more than twice the average from PTV in the case of mouse 2, in which the PTV plane was far from the PVS centerline (*SI Appendix*). The discrepancy is explained by the fact that in a viscous flow, fluid far from the centerline moves slowly. Estimating average velocities using uniformly distributed AIV inferences avoids sampling bias. Being able to more accurately estimate the mean velocity in the 3D PVS, rather than the mean velocity in a single plane, may clarify the existence of differences in CSF flow with aging, Alzhiemer's disease, and hypertension.

AIV-inferred total PVS volume flow rates agree with previous estimates. Using AIV, we infer a volume flow rate of around 2.25×10^4 $\mu m^3/s$ (or 1.35×10^{-3} μL/min) in one side of the pial PVS in the territory of the middle cerebral artery of mouse 1. (Each of the subdomains we considered included only one side of the PVS, as illustrated in Fig. 1*D*). This half of the PVS has a cross-sectional area of 1.1×10^3 μm^2. Ray et al. estimate that the total periarterial cross-sectional area in the murine brain is 0.2 mm^2, or approximately 182 times larger than the section we measured (5). If we assume that the flow rate in the section we measure is typical, we can approximate a total PVS flow rate of 0.25 μL/min, or 0.625 μL/(g-min) for a 0.4-g mouse brain, which agrees well with the estimates of 0.5μL/(g-min) inflow in mice from Ray et al. (5). A total flow rate of 0.625 μL/(g-min) also agrees with an estimate of the upper limit of lymph flow in rat heart muscle (0.45-0.48 μL/(g-min) (56), suggesting that this estimate is reasonable for metabolically active tissue. This work measures volume flow rates in PVSs in vivo, and the measurement is consistent with estimates of total CSF flow in these spaces.

Conservation of mass implies that for a bounded PVS, the volume flow rate Q through every cross-section must be identical, but we observed variation of Q along PVSs. Among the possible causes of variation are uncertainty in PTV measurements and the PVS boundary, including the assumption of stationary boundaries, imperfect AIV optimization, numerical errors associated with the discretized grid, and actual leakage of fluid from the PVS. Our direct numerical simulations of flow in a PVS are independent of PTV measurements and use closed boundaries, excluding measurement uncertainties and leaks. In that case, the volume flow rate inferred by AIV differed between inlet and outlet by just 1.63%. We expect the mismatch due to combined effects of imperfect AIV optimization and grid discretization to be similar in other cases because their grid spacing is similar.

However, in mouse 2 and mouse 4, we observed much larger mismatches, along with tracer and microspheres lying outside the region defined as PVS, at the point where Q decreased sharply (*SI Appendix*, Fig. S5). Together, those observations suggest either that the region we classified as PVS, according to tracer fluorescence, failed to encompass the entire PVS; or that fluid was leaking out of PVSs. It has been suggested that stomata (leptomeningeal fenestrations/pores) might allow fluid to enter PVSs (57, 58). It is also possible that portions of the dura were damaged during surgery, allowing leaks. In future work, AIV could be used to estimate the rate of CSF leakage through stomata by measuring axial changes in volume flow rate. AIV could also be used to estimate flow rates into penetrating PVSs by measuring differences in volume flow rate at axial locations upstream and downstream of the penetrating PVS to infer how much fluid entered the penetrating PVS. Either estimate would significantly improve models of perivascular flow (18) and could help resolve controversies regarding the glymphatic model (1, 6).

AIV-inferred PVS pressure gradients agree with previous estimates. Though pressure gradients in pial PVSs have never been measured previously, those we infer using AIV are consistent with estimates based on models of PVS flow and measurements in other regions of the brain. Kedarasetti et al. predicted that a pressure gradient of 2.7×10^{-4} Pa/μm (2 mmHg/m) would drive a flow with a net velocity of 20 μm/s in pial PVSs (59). Daversin-Catty et al. predicted that a pressure gradient of 1.95×10^{-4} Pa/μm (1.46 mmHg/m) would drive flows with velocities of 30 to 40 μm/s (60). Vinje et al. measured pressure gradients around 1 to 4×10^{-4} Pa/μm (1 to 3 mmHg/m) between the subdural and intraventricular compartments in humans (61). These pressure gradients are all consistent with the pressure gradients of 0.7 to 5×10^{-4} Pa/μm (0.5 to 4 mmHg/m) inferred with AIV.

One advantage of AIV is that it infers the pressure gradients that drive the flow, which are difficult to measure using pressure probes. Being small, those instantaneous pressure gradients can be obfuscated in measurements by the large temporal variations in pressure. Intracranial pressure pulses at both the cardiac and respiratory frequencies (61, 62) in the brain's fluid cisterns. (Pressure has never been measured in PVSs.) Those variations have amplitude 100 to 400 Pa (1 to 3 mmHg) in mice (63), 250 to 1,000 Pa (2 to 8 mmHg) in humans (61, 64–66), and 600 Pa (4.5 mmHg) in alligators (67). Thus, temporal pressure variations are three orders of magnitude larger than spatial variations across a short section of PVS, inferred by AIV to be on the order of 0.1 Pa (7.5×10^{-4} mmHg). However, temporal pressure variations drive no flow, whereas gradients do (as is evident in Eq. **2**). The gradients, though small, are key for understanding and predicting CSF dynamics in PVSs. Because AIV infers pressure using Eq. **2**, it captures the important variations associated with instantaneous gradients while excluding the less-important large

temporal variations. This selectivity is an advantage of AIV. Even if pressure measurements in PVSs (and at multiple PVS locations) become possible in the future, if those measurements are referenced to atmospheric pressure and therefore capture the large temporal variations, extracting the small gradients will require great sensitivity. For example, the average intracranial pressure in mice is approximately 300 Pa (2 mmHg), so measuring gradients of 5×10^{-4} Pa/μm (4 mmHg/m) between locations separated by 100 μm would require measuring pressure differences of 0.05 Pa (4×10^{-4} mmHg).

The pressure oscillations in the PVS at the cardiac frequency that we report are not expected to measurably deform the parenchyma. Kedarasetti et al. (68) and Bojarskaite et al. (69) observed deformations of parenchymal tissue surrounding penetrating PVSs, at timescales associated with slow or ultraslow vasomotion. Based on a pressure difference of 30 Pa (0.23 mmHg) inducing a 1% strain (70), we can estimate the modulus of elasticity for parenchymal tissue as 3000 Pa, in close agreement with other published estimates, which range from 500 to 10,000 Pa (71). AIV infers pressure fluctuations of around 0.1 Pa (7.5×10^{-4}) at the cardiac frequency (Fig. 4*C*). If we assume a modulus of 500 Pa, at the low end of the various estimates, this would result in a strain of around 2×10^{-4} in the parenchyma, a level that would not be detectable with current in vivo imaging techniques. That prediction is consistent with our observations, which reveal negligible parenchymal deformation at the cardiac frequency. The deformations observed by Kedarasetti et al. and Bojarskaite et al. suggest the presence of larger amplitude pressure oscillations at lower frequencies and in penetrating PVSs. Indeed, Kedarasetti et al. predicted pressure oscillations in a penetrating PVS with an amplitude of 15 Pa (0.1 mmHg) resulting from functional hyperemia (70).

The mice used in this study were healthy, wild-type mice, but AIV can be applied to explore how PVS flow is altered in various conditions, including disease and aging as has been done with PTV (12, 24, 72), and could potentially be incorporated into models of disease pathogenesis to determine whether the forces induced by PVS flow play a role in disease progression. We speculate about a few possible applications here.

Vascular amyloidosis, aging, and small vessel disease all cause long-term remodeling of the PVS (73), and AIV could be used to determine how the altered PVS lumen affects flow rates, pressure gradients, and shear stress. Vascular amyloidosis is characterized by the accumulation of amyloid-β plaques between the smooth muscle cells and the endothelial cells, and in severe cases the plaques can protrude into the PVS lumen, altering PVS flow and potentially inducing harmful flow structures. Detecting flow features would be difficult with single-plane PTV, and determining appropriate inlet and outlet conditions would be difficult with direct numerical simulations (DNS), but AIV can detect the presence of flow features in vivo with streamlines without knowledge of the inlet and outlet conditions.

Small vessel disease (SVD) is characterized by enlarged PVSs, which in isolation would have lower resistance to flow, but small vessel disease results in reduced PVS flow due to changes in other parts of the network. This reduction in flow would not be predicted with DNS without knowledge of how the inlet and outlet conditions change, but would be readily inferred with AIV, since it does not require knowledge of the inlet and outlet conditions. It has been hypothesized that the perivascular space enlargement is a result of inflammation (74) and that enlarged PVSs may play a role in SVD pathogenesis (75). Local inflammation may result from oscillatory pressure exerted on surrounding brain tissue or wall shear stress, both of which can now be inferred in vivo in mouse models with AIV, although enlarged perivascular spaces have not been reported around pial arteries, specifically. Hypertension is associated with SVD and can cause arterial wall stiffening, which may alter oscillations in pressure and wall shear stress in the perivascular spaces. The way a stiff blood vessel impacts the pressure and wall shear stress inside the adjacent PVS can also be inferred with AIV without knowledge of the vessel material properties. The cause and impact of enlarged PVSs is unknown, and these hypothesis are speculative but can now be tested with AIV.

Shear induced by fluid flow can promote protein aggregation (76), and though it is unclear how much shear is required to promote the amyloid aggregation that correlates with cerebral amyloid angiopathy and Alzheimer's disease (49–51, 77), recent measurements suggest that the shear rates we infer with AIV may be in the relevant range (76, 78). The idea that shear in pial PVSs may contribute to amyloid aggregation between the smooth muscle cells and endothelial cell wall or in the parenchyma is speculative, and additional work is needed to determine exactly what shear rates promote amyloid aggregation and under what conditions. However, the point is that AIV can be used to determine the shear conditions that exist in vivo, opening the possibility to explore the role shear plays in physiological and pathological conditions.

Wall shear stress is important in cardiovascular flows due to its role in regulating blood flow and vessel wall remodeling (40–45). Magnitudes vary with location and physiological state but are on the order of 1.5 Pa (46). In lymph vessels, wall shear stress may modulate lymphatic tone and pumping (47, 48) and has peak magnitude around 0.3 to 1.2 Pa in mesenteric lymph vessels (47, 48). The wall shear stresses we infer in pial PVSs have average and peak magnitudes around 0.005 and 0.03 Pa, respectively. Whether wall shear stress plays an important role in PVSs, as does it in blood vessels and lymph vessels, is not known, in part because its details have not been quantified before. One speculation is that perivascular flows may influence smooth muscle cells through mechanotransduction. The inner boundary of any PVS is lined with smooth muscle cells. They are known to experience mechanotransduction from interstitial flows (41, 79) and may likewise experience it from perivascular flows, which impose shear stresses of similar magnitude (80). Though that magnitude is lower than for blood flow, the CSF is in direct contact with the smooth muscle cells, whereas the blood is typically only in contact with endothelial cells. A separate speculation is that a portion of the outer boundary of a pial PVS is directly adjacent to brain tissue, which may be sensitive to oscillatory pressures and shear stress. In general, shear stress can induce changes in gene expression and inflammation (4). It is not clear what affect the wall shear stress has on the outer boundaries of the PVS, but now it can be measured with AIV. The outer boundary of a penetrating (but not pial) PVS is lined with astrocytes with receptors that may allow Ca^{2+} entry in response to shear stresses (81). By inferring shear stress in vivo, AIV can enable future studies of the effects of perivascular shear stress.

There are several important limitations in our experimental measurements and AIV inferences. First, when performing AIV, we approximated PVS boundaries as stationary, though they fluctuate, particularly at the cardiac frequency, as previously reported (24) and shown in *SI Appendix*, Fig. S14. The motion over the course of a cardiac cycle is approximately one μm, of similar magnitude to the uncertainty in PVS wall location (*SI Appendix*, Fig. S4). Artery wall fluctuations create cross-stream oscillatory

fluid motions observable via PTV, and are linked to downstream pulsatile fluid motion (24). Despite having stationary boundaries, the AIV inferences correctly include oscillatory cross-stream fluid motion pulsatile downstream fluid motion. In future work, 3D boundary motion could be inferred by measuring in-plane boundary motion, then assuming axisymmetric vessel dilation and contraction. Second, phase merging precludes the possibility of exploring frequencies lower than the cardiac frequency. Though the cardiac frequency is the dominant frequency, CSF in PVSs may also oscillate at the respiratory frequency and at frequencies corresponding to slow and very slow waves (24, 69). To capture these lower frequencies, particle density would need to be higher so that phase merging is not required.

We report volume flow rates, pressures, and wall shear stresses inferred in in vivo murine PVSs, inferred using both measurements and theory. These numbers are immediately useful in modeling flow in PVSs, and AIV can in the future potentially be used to address critical questions related to cerebral CSF flow including estimating volume flow rates in penetrating PVSs and through pial PVS walls and exploring the role CSF flow-induced shear stress plays in healthy and diseased conditions. With the ability to infer volume flow rates (as opposed to sparse, single-plane velocity measurements) and streamlines, AIV may be able to elucidate how aging and disease affect PVS flow.

Materials and Methods

Animals and Surgical Preparation. Wild-type mice were anesthetized with ketamine/xylazine and cranial windows were installed. One-micron fluorescent microspheres were injected into the cisterna magna to track CSF flow, and mice received intracisternal and intravenous injections of Alexa Fluor 647-conjugated bovine serum albumin (66.5 kDa) and an intravenous injection of FITC-conjugated dextran (2,000 kDa) to show the location of the PVS and blood vessel lumen. Additional information on the mice and surgical procedures can be found in *SI Appendix*.

Measurement of Vital Signs. Heart rate and respiration were acquired at 1 kHz using a small animal physiological monitoring device (Harvard Apparatus). The signal was digitized and recorded with a DigiData 1550A digitizer and AxoScope software (Axon Instruments).

In Vivo Two-Photon Laser Scanning Microscopy. Two-photon imaging was performed using a resonant scanner Bergamo scope (Thorlabs) and a Chameleon Ultra II laser (Coherent) with a water-immersion 20x objective (1.0 NA, Olympus). Intravascular FITC-dextran and either red microspheres or BSA-647 were excited at an 820-nm wavelength, and emission was filtered at 525, 607, and 647 nm. Images were acquired at 30 Hz (ThorSync software) simultaneously with physiological recordings (3 kHz, ThorSync software). For mouse 1, images were acquired for one minute at two planes, referred to as Planes A and B. Plane A is shown in Fig.1*C*. Plane B is approximately 20 μm below Plane A. In order to determine how much the flow varied while acquiring data in the different planes, Plane A was reacquired after imaging plane B. For mice 2 to 4, images were acquired for 6 min. To visualize the PVS shape, a volume scan of the region was imaged with 512 × 512 pixel frames from the surface to a depth of 200 μm with 1-μm steps.

Particle Tracking Velocimetry. We performed particle tracking velocimetry on the microspheres in the time series images from the two-photon laser scanning microscopy. We tracked the motion of each microsphere through time and calculated its velocity based on its changing position with subpixel accuracy as described by Mestre et al. (12, 24) using automated MATLAB code following a previously described algorithm (82, 83). We calculated the particle velocities by convolving a Gaussian smoothing and differentiating kernel with the tracked particle positions in each frame, which allows us to achieve subframe accuracy in the particle velocity.

PVS Segmentation. The three-dimensional boundaries of the PVS were constructed by segmenting the PVS based on the location of the fluorescent tracer in the CSF inside the PVS. Image resolution in the transverse plane was 0.648 μm/pixel, while resolution in the dimension aligned with cortical depth was 1 μm/pixel. Images were upsampled in the cortical depth dimension (z) so that the image resolution was isotropic and then smoothed with a 3D Gaussian filter with SD of two voxels. The fluorescent signal intensity detected by the microscope varies with depth because the signal is attenuated as it passes through tissue, so we binarized the volume using a depth-varying threshold. We determined six different depth-varying thresholds, resulting in six different geometries, G1–G6, for the geometry sensitivity analysis on mouse 1. For G1 the threshold was equal to the sum of the mean and SD of the image intensity at each depth. Unless otherwise noted, all domains shown are from G1 from mouse 1. For G2 and G3, the threshold was determined based on the location of the maximum image intensity gradient. We used the edge3 command in MATLAB to identify the maximum gradient. We used an edge sensitivity of 0.5 for G2 and 0.05 for G3. At each depth, the threshold was set equal to the median intensity value at the edges in the image. G4 and G5 were obtained by manually combining the depth-varying thresholds determined for G1–G3 in different ways, as shown in *SI Appendix*, Fig. S4*A*. The threshold for G6 was the highest threshold from G1 to G5 at each depth. For all geometries, the resulting volume was smoothed using a 3D box filter that had a kernel size of nine voxels. The outer boundary of the G1 segmentation is shown in Fig. 1 *C* and *D*.

We followed the same process for determining the 3D boundaries for the other three mice, but we performed AIV for only one geometry from each mouse. The depth-varying threshold was iteratively adjusted by tuning the parameters used to determine the threshold until the boundary in the imaging plane most closely matched the location of the particles.

Registration of Particle Tracking Images to Volume Scan. The 2D time-series images showing particle motion were registered to the isotropic 3D image in order to determine the cortical depth at which each time series was acquired and to identify any translation or rotation of the field of view between the acquisition of the 2D time series and the 3D volume scans. The time-series images were acquired in approximately the same transverse (x-y) location as the volume images, but were shifted by a few microns. We found that the field of view for the time-series images shifted slightly over the course of the data acquisition, so we performed a dynamic registration by averaging and registering groups of 25 images. We used the following algorithm for 2D-to-3D registration. First, we determined the depth at which each 2D image was acquired by finding the value of k that minimizes the difference d_k between the time series image $I_{2D,ij}$ and each 2D image extracted from the 3D volume series $I_{3D,ijk}$:

$$d_k = \frac{\sum_i^M \sum_j^N |I_{2D,ij} - I_{3D,ijk}|}{\sum_i^M \sum_j^N I_{3D,ijk}}, \quad [1]$$

where i and j correspond to the dimensions in the transverse plane (x-y) and k corresponds to the dimension into the cortex z, and M and N are the number of voxels in each dimension in the transverse plane. Second, we found the in-plane rigid transformation (translation and rotation) between the time series and the image from the volume series, using the MATLAB imregtform function. Last, we applied the transformation to the time-series image and recalculate the difference d_k for every image in the volume series. If a new value of k minimizes d_k, repeat until the value k does not change following the planar transformation.

Subdomain . For the AIV training and testing, we consider only a portion of the imaged domain, as indicated in Fig. 1 *C*–*E*.

Phase Merging. The number of particles in each image in the time series is relatively small, but flows in PVSs are pulsatile and closely synchronized with the cardiac cycle (24). We divided the cardiac cycle into 50 phases, then combined all the particles that appear at the same cardiac phase, thus increasing the effective density of the particles, as shown in *SI Appendix*, Fig. S1.

Underlying Physical Laws. The flow of cerebrospinal fluid along a PVS is incompressible and obeys the Navier–Stokes and continuity equations (7, 84):

$$\rho\left(\frac{\partial \mathbf{u}}{\partial t} + \mathbf{u}\cdot\nabla\mathbf{u}\right) = -\nabla p + \mu\nabla^2\mathbf{u}, \qquad \nabla\cdot\mathbf{u} = 0, \qquad [2]$$

where $\mathbf{u} = (u, v, w)$ is the Eulerian velocity field, ρ is the fluid density, p is the fluid pressure, μ is the dynamic viscosity, ∇ is the spatial gradient operator, and ∇^2 is the Laplacian operator. We assume that the density and viscosity are constant and uniform, with $\rho = 993$ kg/m^3 and $\mu = 6.95 \times 10^{-4}$ Pa s. The kinematic viscosity $\nu \equiv \mu/\rho$ is 7×10^{-7} m^2/s. These equations are supplemented by the no-slip boundary condition $\mathbf{u} = 0$ at the walls of the PVS.

The Navier–Stokes equation Eq. **2** that we use does not include the gravity force. As is usual, the pressure in this equation is defined to be the total pressure minus the hydrostatic pressure (which balances the gravity force), and the hydrostatic equation is subtracted from the full NS equation. In vivo measurements of pressure at various locations in the brain would give the total pressure, which will include the hydrostatic pressure variation.

Implicit in these equations is the assumption that pial PVSs are open, not porous. Flow characteristics measured in vivo broadly support that assumption (25).

Artificial Intelligence Velocimetry. AIV is developed based on physics-informed neural networks (PINNs), which can assimilate velocity vectors from PTV and the underlying physical laws. In the context of AIV, a neural network $\mathcal{F}_{NN}$ is used to approximate the solution of the flow fields, namely:

$$(\mathbf{u}, p) = \mathcal{F}_{NN}(\mathbf{x}, t, \Theta), \qquad [3]$$

where $\mathcal{F}_{NN}$ receives the coordinates ($\mathbf{x} = (x, y, z) \in \mathbb{R}^3$ and t) as input and Θ denotes the learnable parameters in the network; $\mathbf{u}(\mathbf{x}, t, \Theta) = (u, v, w)$ and $p(\mathbf{x}, t, \Theta)$ are the velocity and pressure fields inferred by the networks, respectively. Here, $\mathcal{F}_{NN}$ is instantiated by using a feed-forward fully connected network, where Θ include the weights and biases of multiple hidden layers. In order to train the parameters Θ, we apply the phase-merged PTV data $\mathcal{D}$ as labels and minimize the mean squared loss as follows:

$$\mathcal{L}_{data}(\Theta) = \frac{1}{N}\sum_{n=1}^{N}\left(u^n_{PTV} - u(\mathbf{x}^n, t^n, \Theta)\right)^2 + \frac{1}{N}\sum_{n=1}^{N}\left(v^n_{PTV} - v(\mathbf{x}^n, t^n, \Theta)\right)^2. \qquad [4]$$

This penalizes the mismatch between the data $(u, v)_{PTV}$ and the network output; $\sum_{n=1}^{N}$ is the summation over different data points and N is the batch size for one training iteration. The data loss $\mathcal{L}_{data}$ allows us to anchor the solution (i.e., flow fields) based on the measurements from PTV. However, it does not guarantee good estimation at the locations where the velocity data are not available because of the sparsity. Therefore, another loss function penalizing the residuals of the governing equations is introduced in AIV:

$$\mathcal{L}_{res}(\Theta) = \frac{1}{N}\sum_{i}\sum_{n=1}^{N}\left(\mathbf{e}_i(\mathbf{x}^n, t^n, \Theta)\right)^2, \qquad [5]$$

where $\mathbf{e}_{i=1,2,3,4}$ includes the residuals of three-dimensional Navier–Stokes equations and the continuity equation. The partial differential operators in the governing equations are computed using automatic differentiation (AD) (85), which calculates the derivatives of the outputs with respect to the network inputs directly in the computational graph. In addition, the no-slip boundary conditions on the PVS are also enforced by adding:

$$\mathcal{L}_{bcs}(\Theta) = \frac{1}{N}\sum_{\mathbf{u}=(u,v,w)}\sum_{n=1}^{N}\left(\mathbf{u}(\mathbf{x}^n, t^n, \Theta)\right)^2, \qquad [6]$$

where $\mathbf{x} \in \partial\Omega$ represents points at the boundary. In summary, the total loss function of AIV can be defined as:

$$\mathcal{L}(\Theta) = \lambda_d\mathcal{L}_{data} + \lambda_r\mathcal{L}_{res} + \lambda_b\mathcal{L}_{bcs}, \qquad [7]$$

where λ_* are the weighting coefficients used to balance different terms in the loss function. Our objective is to find a neural network, $\mathcal{F}_{NN}(\Theta)$, to approximate the velocity and pressure fields, which satisfy the PTV data as well as the physical laws. The hyperparameter settings in AIV can be found in *SI Appendix*.

Computational Fluid Dynamics Simulation. We performed a synthetic experiment to validate the AIV methodology, as shown in *SI Appendix*, Figs. S2 and S3. We simulated steady perivascular flow at Reynolds number $Re = 2.2 \times 10^{-3}$ using a high-order spectral element method. The 3D geometry was reconstructed from two-photon images of a mouse perivascular space. We used a tetrahedral mesh with 81,375 elements. Doubling the number of elements resulted in the same steady flow field. We prescribe a Poiseuille inflow velocity profile, a zero-pressure outlet boundary condition, and no-slip boundary conditions on the walls. The dimensionless time step size is 1×10^{-5}, and the simulation continued until the L2 norm of the velocity was steady, which occurred at computational time is 20. We extracted 2D velocity vectors from the simulated flow fields and applied AIV to infer the 3D flow fields.

Velocity Calculations. The time-averaged and normalized speed plots in *SI Appendix*, Figs. S11*C*, S11*D*, S13*C* and S13*D* were calculated by dividing the spatial domain into 7.5×7.5 pixel bins, then time-averaging the velocities in each bin. Subsequently, the velocities were normalized by the maximum velocity over the space. The Rms velocity (u_{RMS}) was computed by calculating the Rms velocity of all the particles or AIV-inferred velocities in each frame or phase. We calculated the downstream velocity, or downstream velocity component $u_{down} = u \cdot |\hat{u_{mean}}|$, where u is the instantaneous velocity and $|\hat{u_{mean}}|$ is a unit vector computed from time-averaging the velocity field over the entire time series. In Fig. 2*E*, we show the spatial average of all the downstream velocity components. The cross-stream velocity u_{cross} is the flow component perpendicular to the downstream velocity component and was obtained similarly, as a dot product of the velocity of each particle and a unit vector perpendicular to the local mean velocity. The Rms and downstream velocities reported for particle tracking data include only velocities from particles within the segmented 3D domain and subdomain, as shown in Fig. 1*E*.

The Rms error between the AIV inferred velocities and the PTV data is defined as

$$\mathrm{RMSE}_{mean} = \sqrt{\frac{1}{N}\sum_{i}^{N}[(u_{PTV} - u_{AIV})^2 + (v_{PTV} - v_{AIV})^2]}, \qquad [8]$$

and the root-median-square error is defined as

$$\mathrm{RMSE}_{med} = \sqrt{\mathrm{median}[(u_{PTV} - u_{AIV})^2 + (v_{PTV} - v_{AIV})^2]}, \qquad [9]$$

where (u_{PTV}, v_{PTV}) and (u_{AIV}, v_{AIV}) are the two-dimensional PTV and AIV velocities in the PTV measurement plane, computed over all points in space and time.

We compute the percent error for each as

$$\frac{\text{root-mean-square error error}}{\sqrt{\frac{1}{N}\sum_{i}^{N}(u^2_{PTV} + u^2_{PTV})}}, \qquad [10]$$

and

$$\frac{\text{root-median-square error}}{\sqrt{\mathrm{median}(u^2_{PTV} + u^2_{PTV})}}. \qquad [11]$$

In addition, the relative L_2-norm error is defined as $\frac{\|x_{AIV} - x_{CFD}\|_2}{\|x_{CFD}\|_2}$ where x is the quantity of interest at all points in space, and $\|x\|_2$ is the L_2-norm of x.

Hydraulic Resistance.

Computational fluid dynamics. The direct simulations were performed in NX Flow in NX Advanced Simulation software from Siemens PLM. We prescribed a steady flow at the inlet, similar to the time-averaged flow rate inferred by AIV. We created a Poiseuille velocity profile at the inlet of the PVS by extruding the shape of the PVS at the inlet until the flow was fully developed. We set a zero-pressure outlet boundary condition and no-slip boundary conditions on the walls. The computational grid was refined until resistance changed by less than 0.1% when halving the element size, which occurred when the element size was 0.2 μm. We calculated the resistance by dividing the difference between the average pressure at planes located 10 μm from the ends of the domain by the distance d between the planes and the prescribed volume flow rate, $R = \frac{P_{\text{inlet}} - P_{\text{outlet}}}{d \cdot Q}$.

Resistance for Poiseuille flow in channels of constant cross-section. To estimate hydraulic resistance and its axial variation, without the computational cost of simulating the Navier–Stokes equations, we divided the PVS subdomain into short segments and calculated the resistance of each, assuming fully developed flow. We solved the Poisson equations that describe such flows numerically with MATLAB's solvepde. For each cross-section, we first eroded the binary array containing the PVS segmentation by one pixel then found the location of the segmented PVS boundary using MATLAB's bwboundaries. We used the polyshape and geometryFromMesh commands to create a model that can be discretized using MATLAB's generateMesh command, which creates a triangular mesh. We refine the grid until the element size is small enough that error in resistance for a circle of the same area is less than 1%.

We calculated the resistance in a channel with an elliptical annular cross-section using the equation for the resistance of an optimal elliptical annulus described by Tithof et al. (53). The shape is determined to be optimal because it minimizes the resistance for a given ratio K of PVS-to-vessel cross-sectional areas: $R = 2 \cdot 6.67 \mu K^{-1.96} / r^4$. Here μ is the dynamic viscosity and r is the vessel radius, which we determined based on the segmented PVS area and an area ratio K=1.4, which has been shown to be a representative value for pial PVSs (24). We multiplied the equation provided in ref. 53 by two to obtain the resistance of half of the annulus, since we consider only the resistance in one side of the PVS. The resistance in a channel with a circular cross-section is given by $R = \frac{8\mu}{\pi r^4}$.

Oscillatory to Mean Calculations. The ratio of oscillatory to mean quantities is taken to be the difference between the maximum and minimum values divided by the mean of the time-varying, spatially averaged quantity over the course of the cardiac cycle:

$$ratio = \frac{\max X - \min X}{(1/N) \cdot \sum_i^N X}, \quad [12]$$

where X is the quantity of interest (flow rate, shear, or pressure) and N is the number of measurements.

Shear Stress Calculations. The shear stress is defined as

$$\tau = \mu \dot{\gamma}, \quad [13]$$

where $\dot{\gamma}$ is the shear rate, calculated using the stress–strain rate tensor $\mathbf{E}$:

$$\dot{\gamma} = \sqrt{2\mathbf{E} : \mathbf{E}}, \qquad \mathbf{E} = \frac{1}{2}(\nabla \mathbf{u} + (\nabla \mathbf{u})^T). \quad [14]$$

The gradients of the velocity field were computed in the neural network via automatic differentiation. The resulting shear stress has physical units of Pascal. By this definition, τ is a scalar magnitude accounting for all components of shear, not just the component oriented downstream along the wall (often called the "wall shear stress"). We expect that if signaling at the PVS wall and/or aggregation of plaques are affected by shear, the magnitude is the relevant quantity. That said, in these laminar flows, we also expect the magnitude to be dominated by the component proportional to the wall-normal gradient of the downstream velocity.

Data, Materials, and Software Availability. Data have been deposited in Zenodo (https://zenodo.org/record/7723381#.ZAzSZjpKhD8) (86).

ACKNOWLEDGMENTS. G.E.K. acknowledges support by the OSD/AFOSR MURI grant FA9550-20-1-0358, United States of America. D.H.K., J.H.T., and M.N. acknowledge support from the United States Army grant MURI W911NF1910280 and the NIH grant U19NS128613. D.H.K., J.H.T., M.N., and G.E.K. acknowledge support the NIH grant R01AT012312. We thank Yiming Gan for assistance with the particle tracking, Aditya Raghunandan for helpful discussion regarding the potential physiological impact of shear, and Dan Xue for help with graphic design on Fig. 1*A*.

Author affiliations: [a]Department of Mechanical Engineering, University of Rochester, Rochester, NY 14627; [b]Institute of Cyber-Systems and Control, College of Control Science and Engineering, Zhejiang University, Hangzhou 310027, Zhejiang, China; [c]Center for Translational Neuromedicine and Department of Neuroscience, University of Rochester Medical Center, Rochester, NY 14627; [d]Department of Mathematics, College of Information Science and Technology, Jinan University, Guangzhou 510632, China; [e]School of Pharmacy, China Medical University, Shenyang, Liaoning 110122, China; [f]Division of Applied Mathematics, Brown University, Providence, RI 02912; and [g]School of Engineering, Brown University, Providence, RI 02912

Author contributions: K.A.S.B., S.C., J.H.T., M.N., G.E.K., and D.H.K. designed research; K.A.S.B., S.C., A.L.-d.-G., J.S., X.Z., and T.D. performed research; K.A.S.B. and S.C. analyzed data; and K.A.S.B., S.C., A.L.-d.-G., J.H.T., M.N., G.E.K., and D.H.K. wrote the paper.

Competing interest statement: S.C. and G.E.K. have filed a patent application based on some of the research presented in this manuscript.

This article is a PNAS Direct Submission. A.M. is a guest editor invited by the Editorial Board.

1. S. Hladky, M. A. Barrand, The glymphatic hypothesis: The theory and the evidence. *Fluids Barriers CNS* **19**, 9 (2022).
2. J. M. Tarasoff-Conway *et al*., Clearance systems in the brain-implications for Alzheimer disease. *Nat. Rev. Neurol.* **11**, 457–470 (2015).
3. A. A. Linninger, K. Tangen, C. Hsu, D. Frim, Cerebrospinal fluid mechanics and its coupling to cerebrovascular dynamics. *Ann. Rev. Fluid Mech.* **48**, 219–257 (2016).
4. M. K. Rasmussen, H. Mestre, M. Nedergaard, Fluid transport in the brain. *Physiol. Rev.* **102**, 1025–1151, PMID: 33949874 (2022).
5. L. A. Ray, J. J. Heys, Fluid flow and mass transport in brain tissue. *Fluids* **4**, 196 (2019).
6. T. Bohr *et al*., The glymphatic system: Current understanding and modeling. *iScience* **25**, 104987 (2022).
7. D. H. Kelley, J. H. Thomas, Cerebrospinal fluid flow. *Annu. Rev. Fluid Mech.* **55**, null (2023).
8. B. T. Kress *et al*., Impairment of paravascular clearance pathways in the aging brain. *Ann. Neurol.* **76**, 845–861 (2014).
9. Q. Ma, B. V. Ineichen, M. Detmar, S. T. Proulx, Outflow of cerebrospinal fluid is predominantly through lymphatic vessels and is reduced in aged mice. *Nat. Commun.* **8**, 1434 (2017).
10. W. Peng *et al*., Suppression of glymphatic fluid transport in a mouse model of Alzheimer's disease. *Neurobiol. Dis.* **93**, 215–225 (2016).
11. S. D. Mesquita *et al*., Functional aspects of meningeal lymphatics in ageing and Alzheimer's disease. *Nature* **560**, 185–191 (2018).
12. H. Mestre *et al*., Cerebrospinal fluid influx drives acute ischemic tissue swelling. *Science* **367** (2020).
13. X. B. Ding *et al*., Impaired meningeal lymphatic drainage in patients with idiopathic Parkinson's disease. *Nat. Med.* **27**, 411–418 (2021).
14. G. Ringstad, S. A. S. Vatnehol, P. K. Eide, Glymphatic MRI in idiopathic normal pressure hydrocephalus. *Brain* **140**, 2691–2705 (2017).
15. T. Taoka *et al*., Evaluation of glymphatic system activity with the diffusion MR technique: Diffusion tensor image analysis along the perivascular space (DTI-ALPS) in Alzheimer's disease cases. *Japan. J. Radiol.* **35**, 172–178 (2017).
16. P. K. Eide, V. Vinje, A. H. Pripp, K. A. Mardal, G. Ringstad, Sleep deprivation impairs molecular clearance from the human brain. *Brain* **144**, 863–874 (2021).
17. J. Tithof *et al*., A network model of glymphatic flow under different experimentally-motivated parametric scenarios. *iScience* **25**, 104258 (2022).
18. K. A. S. Boster, J. Tithof, D. D. Cook, J. H. Thomas, D. H. Kelley, Sensitivity analysis on a network model of glymphatic flow. *J. R. Soc. Interface* **19**, 20220257 (2022).
19. V. Ratner *et al*., Cerebrospinal and interstitial fluid transport via the glymphatic pathway modeled by optimal mass transport. *NeuroImage* **152**, 530–537 (2017).
20. S. Koundal *et al*., Optimal mass transport with Lagrangian workflow reveals advective and diffusion driven solute transport in the glymphatic system. *Sci. Rep.* **10**, 1–18 (2020).
21. X. Chen *et al*., Cerebral amyloid angiopathy is associated with glymphatic transport reduction and time-delayed solute drainage along the neck arteries. *Nat. Aging* **2**, 214–223 (2022).
22. J. J. Iliff *et al*., A paravascular pathway facilitates CSF flow through the brain parenchyma and the clearance of interstitial solutes, including amyloid β. *Sci. Transl. Med.* **4**, 147ra111 (2012).
23. B. A. Plog, M. Nedergaard, The glymphatic system in central nervous system health and disease: Past, present, and future. *Annu. Rev. Pathol-Mech.* **13**, 379–394 (2018).
24. H. Mestre *et al*., Flow of cerebrospinal fluid is driven by arterial pulsations and is reduced in hypertension. *Nat. Commun.* **9**, 4878 (2018).
25. F. Min Rivas *et al*., Surface periarterial spaces of the mouse brain are open, not porous. *J. R. Soc. Interface* **17**, 20200593 (2020).
26. A. Raghunandan *et al*., Bulk flow of cerebrospinal fluid observed in periarterial spaces is not an artifact of injection. *eLife* **10**, e65958 (2021).
27. K. D., G. Iaccarino, H. Xiao, Turbulence modeling in the age of data. *Annu. Rev. Fluid Mech.* **51**, 357–377 (2019).

28. S. L. Brunton, B. R. Noack, P. Koumoutsakos, Machine learning for fluid mechanics. *Annu. Rev. Fluid Mech.* **52**, 477–508 (2020).
29. J. Ling, A. Kurzawski, J. Templeton, Reynolds averaged turbulence modelling using deep neural networks with embedded invariance. *J. Fluid Mech.* **807**, 155–166 (2016).
30. S. L. Brunton, J. L. Proctor, J. N. Kutz, Discovering governing equations from data by sparse identification of nonlinear dynamical systems. *Proc. Natl. Acad. Sci. U.S.A.* **113**, 3932–3937 (2016).
31. M. Raissi, P. Perdikaris, G. E. Karniadakis, Physics-informed neural networks: A deep learning framework for solving forward and inverse problems involving nonlinear partial differential equations. *J. Comput. Phys.* **378**, 686–707 (2019).
32. D. Kochkov *et al*., Machine learning-accelerated computational fluid dynamics. *Proc. Natl. Acad. Sci. U.S.A.* **118**, e2101784118 (2021).
33. S. Cai, S. Zhou, C. Xu, Q. Gao, Dense motion estimation of particle images via a convolutional neural network. *Exp. Fluids* **60**, 1–16 (2019).
34. C. Lagemann, K. Lagemann, S. Mukherjee, W. Schröder, Deep recurrent optical flow learning for particle image velocimetry data. *Nat. Mach. Intell.* **3**, 641–651 (2021).
35. M. Raissi, A. Yazdani, G. E. Karniadakis, Hidden fluid mechanics: Learning velocity and pressure fields from flow visualizations. *Science* **367**, 1026–1030 (2020).
36. G. E. Karniadakis *et al*., Physics-informed machine learning. *Nat. Rev. Phys.* **3**, 422–440 (2021).
37. S. Cai *et al*., Artificial intelligence velocimetry and microaneurysm-on-a-chip for three-dimensional analysis of blood flow in physiology and disease. *Proc. Natl. Acad. Sci. U.S.A.* **118** (2021).
38. H. Mestre *et al*., Periarteriolar spaces modulate cerebrospinal fluid transport into brain and demonstrate altered morphology in aging and Alzheimer's disease. *Nat. Commun.* **13**, 3897 (2022).
39. M. Karam, H. Janbon, G. Malkinson, I. Brunet, Heterogeneity and developmental dynamics of lyve-1 perivascular macrophages distribution in the mouse brain. *J. Cereb. Blood Flow Metab.* **42**, 1797–1812 (2022). 10.1177/0271678X221101643.
40. V. L. Rayz, A. A. Cohen-Gadol, Hemodynamics of cerebral aneurysms: Connecting medical imaging and biomechanical analysis. *Annu. Rev. Biomed. Eng.* **22**, 231–256, PMID: 32212833 (2020).
41. J. M. Tarbell, Z. Shi, J. Dunn, H. Jo, Fluid mechanics, arterial disease, and gene expression. *Annu. Rev. Fluid Mech.* **46**, 591–614 (2014).
42. J. Cebral, F. Mut, J. Weir, C. Putman, Quantitative characterization of the hemodynamic environment in ruptured and unruptured brain aneurysms. *Am. J. Neuroradiol.* **32**, 145–151 (2011).
43. H. Meng, V. M. Tutino, J. Xiang, A. Siddiqui, High WSS or Low WSS? Complex interactions of hemodynamics with intracranial aneurysm initiation, growth, and rupture: Toward a unifying hypothesis. *Am. J. Neuroradiol.* **35**, 1254–1262 (2014).
44. J. Frösen, J. Cebral, A. M. Robertson, T. Aoki, Flow-induced, inflammation-mediated arterial wall remodeling in the formation and progression of intracranial aneurysms. *Neurosurg. Focus* **47**, E21 (2019).
45. S. N. Lipp *et al*., Computational hemodynamic modeling of arterial aneurysms: A mini-review. *Front. Physiol.* **11** (2020).
46. D. N. Ku, Blood flow in arteries. *Annu. Rev. Fluid Mech.* **29**, 399–434 (1997).
47. D. C. Zawieja, Contractile physiology of lymphatics. *Lymphat. Res. Biol.* **7**, 87–96, PMID: 19534632 (2009).
48. A. A. Gashev, D. Zawieja, Hydrodynamic regulation of lymphatic transport and the impact of aging. *Pathophysiology* **17**, 277–287 (2010).
49. C. N. Trumbore, Shear-induced amyloid formation in the brain: I. Potential vascular and parenchymal processes. *J. Alzheimers Dis.* **54**, 457–470 (2016).
50. C. N. Trumbore, Shear-induced amyloid formation in the brain: Ii. An experimental system for monitoring amyloid shear processes and investigating potential spinal tap problems. *J. Alzheimers Dis.* **59**, 543–557 (2017).
51. C. N. Trumbore, Shear-induced amyloid formation in the brain: Iii. The roles of shear energy and seeding in a proposed shear model. *J. Alzheimers Dis.* **65**, 47–70 (2018).
52. M. M. Faghih, M. K. Sharp, Is bulk flow plausible in perivascular, paravascular and paravenous channels? *Fluids Barriers CNS* **15**, 17 (2018).
53. J. Tithof, D. H. Kelley, H. Mestre, M. Nedergaard, J. H. Thomas, Hydraulic resistance of periarterial spaces in the brain. *Fluids Barriers CNS* **16** (2019).
54. B. Bedussi, M. Almasian, J. de Vos, E. VanBavel, E. N. T. P. Bakker, Paravascular spaces at the brain surface: Low resistance pathways for cerebrospinal fluid flow. *J. Cerebr. Blood F. Met.* **38**, 719–726 (2017). 10.1177/0271678X17737984
55. A. Raghunandan *et al*., Bulk flow of cerebrospinal fluid observed in periarterial spaces is not an artifact of injection. *eLife* **10**, e65958 (2021).
56. E. M. Renkin, H. Wiig, Limits to steady-state lymph flow rates derived from plasma-to-tissue uptake measurements. *Microvasc. Res.* **47**, 318–328 (1994).
57. M. E. Pizzo *et al*., Intrathecal antibody distribution in the rat brain: Surface diffusion, perivascular transport and osmotic enhancement of delivery. *J. Physiol.* **596**, 445–475 (2018).
58. N. J. Abbott, M. E. Pizzo, J. E. Preston, D. Janigro, R. G. Thorne, The role of brain barriers in fluid movement in the CNS: Is there a 'glymphatic' system? *Acta Neuropathol.* **135**, 387–407 (2018).
59. R. Kedarasetti, P. J. Drew, F. Costanzo, Arterial pulsations drive oscillatory flow of CSF but not directional pumping. *Sci. Rep.* **10**, 1–12 (2020).
60. C. Daversin-Catty, V. Vinje, K. Mardal, M. E. Rognes, The mechanisms behind perivascular fluid flow. *PLoS One* **15**, 1–20 (2020).
61. V. Vinje *et al*., Respiratory influence on cerebrospinal fluid flow - a computational study based on long-term intracranial pressure measurements. *Sci. Rep.* **9**, 9732 (2019).
62. V. Kiviniemi *et al*., Ultra-fast magnetic resonance encephalography of physiological brain activity - glymphatic pulsation mechanisms? *J. Cereb. Blood Flow Metab.* **36**, 1033–1045 (2016).
63. M. Uldall *et al*., A novel method for long-term monitoring of intracranial pressure in rats. *J. Neurosci. Methods* **227**, 1–9 (2014).
64. P. K. Eide, Tæhle, Is ventriculomegaly in idiopathic normal pressure hydrocephalus associated with a transmantle gradient in pulsatile intracranial pressure? *Acta Neurochirurg.* **152**, 989–995 (2010).
65. P. K. Eide, S. Holm, W. Sorteberg, Simultaneous monitoring of static and dynamic intracranial pressure parameters from two separate sensors in patients with cerebral bleeds: Comparison of findings. *BioMed. Eng. OnLine* **11**, 66 (2012).
66. G. Ringstad *et al*., Non-invasive assessment of pulsatile intracranial pressure with phase-contrast magnetic resonance imaging. *PLoS One* **12**, 1–17 (2017).
67. B. A. Young *et al*., Variations in the cerebrospinal fluid dynamics of the American alligator (*Alligator mississippiensis*). *Fluids Barriers CNS* **18**, 11 (2021).
68. R. T. Kedarasetti *et al*., Functional hyperemia drives fluid exchange in the paravascular space. *Fluids Barriers CNS* **17**, 1–25 (2020).
69. L. Bojarskaite *et al*., Sleep cycle-dependent vascular dynamics enhance perivascular cerebrospinal fluid flow and solute transport. bioRxiv (2022).
70. R. T. Kedarasetti, P. J. Drew, F. Costanzo, Arterial vasodilation drives convective fluid flow in the brain: A poroelastic model. *Fluids Barriers CNS* **19**, 34 (2022).
71. A. Smillie, I. Sobey, Z. Molnar, A hydroelastic model of hydrocephalus. *J. Fluid Mech.* **539**, 417–443 (2005).
72. T. Du *et al*., Osmotic swelling via cerebrospinal fluid influx drives cerebral edema formation after cardiac arrest. *Brain* **145**, 787–797 (2021).
73. L. M. Hablitz, M. Nedergaard, The glymphatic system: A novel component of fundamental neurobiology. *J. Neurosci.* **41**, 7698–7711 (2021).
74. R. Brown *et al*., Understanding the role of the perivascular space in cerebral small vessel disease. *Cardiova. Res.* **114**, 1462–1473 (2018).
75. H. Mestre, S. Kostrikov, R. Mehta, M. Nedergaard, Perivascular spaces, glymphatic dysfunction, and small vessel disease. *Clin. Sci.* **131**, 2257–2274 (2017).
76. S. I. A. Cohen *et al*., Proliferation of amyloid-β42 aggregates occurs through a secondary nucleation mechanism. *Proc. Natl. Acad. Sci. U.S.A.* **110**, 9758–9763 (2013).
77. J. Dobson *et al*., Inducing protein aggregation by extensional flow. *Proc. Natl. Acad. Sci. U.S.A.* **114**, 4673–4678 (2017).
78. F. Grigolato, C. Colombo, R. Ferrari, L. Rezabkova, P. Arosio, Mechanistic origin of the combined effect of surfaces and mechanical agitation on amyloid formation. *ACS Nano* **11**, 11358–11367, PMID: 29045787 (2017).
79. J. M. Tarbell, L. M. Cancel, The glycocalyx and its significance in human medicine. *J. Int. Med.* **280**, 97–113 (2016).
80. J. M. Tarbell, Z. Shi, Effect of the glycocalyx layer on transmission of interstitial flow shear stress to embedded cells. *Biomech. Mod. Mechanobiol.* **12**, 111–121 (2013).
81. M. M. Maneshi *et al*., Mechanical stress activates NMDA receptors in the absence of agonists. *Sci. Rep.* **7**, 39610 (2017).
82. D. H. Kelley, N. T. Ouellette, Using particle tracking to measure flow instabilities in an undergraduate laboratory experiment. *Am. J. Phys.* **79**, 267–273 (2011).
83. N. T. Ouellette, H. Xu, E. Bodenschatz, A quantitative study of three-dimensional Lagrangian particle tracking algorithms. *Exp. Fluids* **40**, 301–313 (2006).
84. J. H. Thomas, Fluid dynamics of cerebrospinal fluid flow in perivascular spaces. *J. R. Soc. Interface* **16**, 52–57 (2019).
85. A. G. Baydin, B. A. Pearlmutter, A. A. Radul, J. M. Siskind, Automatic differentiation in machine learning: A survey. *J. Mach. Learn. Res.* **18**, 1–43 (2018).
86. K. A. S. Boster, Data from "Artificial intelligence velocimetry reveals in vivo flow rates, pressure gradients, and shear stresses in murine perivascular flows." Zenodo. https://zenodo.org/record/7723381#.ZA-obpFBw2x. Deposited 11 March 2023.